Electronic Supplementary Material (ESI) for Journal of Materials Chemistry C.

Photochemical Synthesis of Dendritic Silver Nano-particles for Anti-counterfeiting

Zhi Zhao,*[ab] Ninad Chamele,[a] Michael Kozicki,[a] Yu Yao[a] and Chao Wang*[ab]

[a] *School of Electrical, Computer and Energy Engineering, Arizona State University, Tempe, Arizona 85287, USA. *E-mail: zzhao71@asu.edu, wangch@asu.edu; Tel: +1 480 965 2056*

[b] *Center for Molecular Design and Biomimetics at the Biodesign Institute, Arizona State University, Tempe, Arizona 85287, USA.*

Material and methods

SIFT analysis. The scale-invariant feature transform (SIFT) analysis method has been published in one of our previous publications.[1] In general, a simplified method of subgraph matching for weighted graphs using Euclidean distance is employed to evaluate similarity between a randomly generated pattern and a set of reference patterns. The analysis process comprises three main stages including image preprocessing, graph representation and graph based authentication. In the image preprocessing stage, the quality of captured image is improved to provide a reliable input for the subsequent stage of graph representation, where the enhanced image is processed and the main skeleton of pattern is extracted. The extracted pattern is then converted to a tree-based graph, where the tree intermediate and leaf nodes are corresponding to the skeleton bifurcation and end points, respectively. Further, a two-element vector is assigned to each edge that represents the Euclidean distance between the respective

parent and child nodes as well as the angle of the branch with respect to a reference direction. The final stage of the framework utilizes a graph matching algorithm to compare the developed graph for the test object with a set of valid graphs in the database in order to examine the validity and identity of the test object.

Results and discussions

A representative region of the Ag dendrites was checked under EDX mapping (Figure S1b-S1d). The result clearly showed that the silver distribution well matched the morphology of the dendrites, while the O distribution has little correlation with the dendritic pattern. This further indicated that the Ag should not be oxidized.

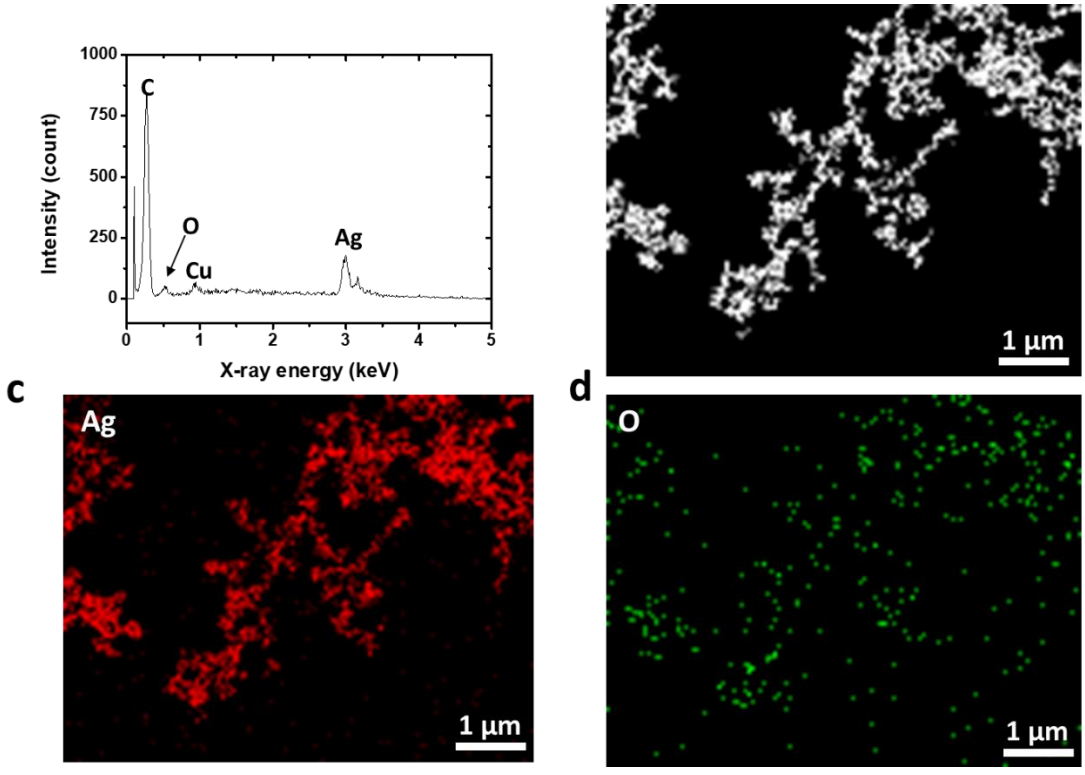

Figure S1. (a) EDX spectrum of the silver dendrites in Figure 2c. (b) A representative region in the dendrites. (c-d) Silver and oxygen element map of (b).

Mechanism of dendritic AgNP formation. We believe it is critical to use polymeric ligands as the polymer backbone acts as a chain to tether AgNPs. In fact, if AAm was used as the ligand and reducing agent, no dendritic particle will form (Figure S2). The polymeric ligand was able to fix the relative positions of adjacent AgNPs, so that interparticle Ag growth could occur. In comparison, AgNPs bound to small molecule ligands were still subject to random movement in the aqueous solution and it is unlikely that two particles could be connected efficiently through crystal growth. It is expected that the relative position of the initially formed AgNPs will be fixed by PAAm chains through chelation (Figure S3). Consequently, the accessibility of different AgNPs for citrate ions will be different. For example, AgNPs located at the edge of polymer chains would have a better chance to keep growing under the presence of the reducing agent. In addition, the local distribution of free amine groups varies for individual AgNPs, leading to an anisotropic growth of Ag under continuous UV illumination.

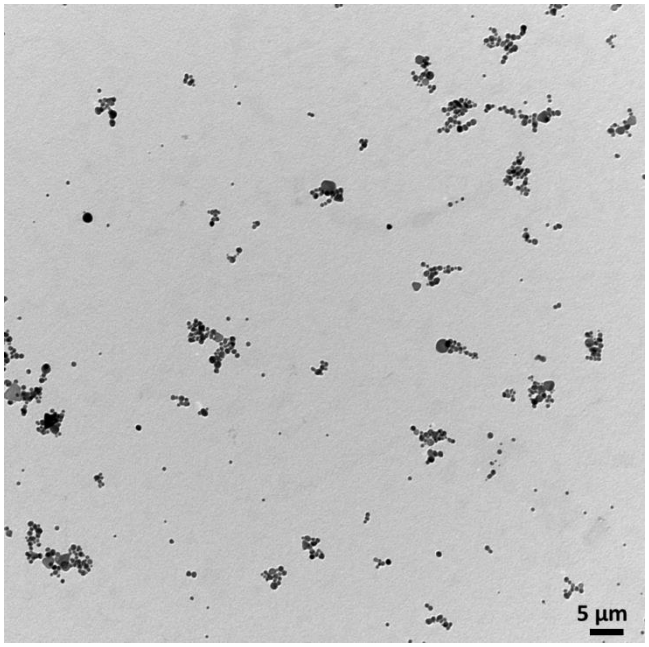

Figure S2. A representative structure showing the molecular structure during the formation of dendritic AgNPs.

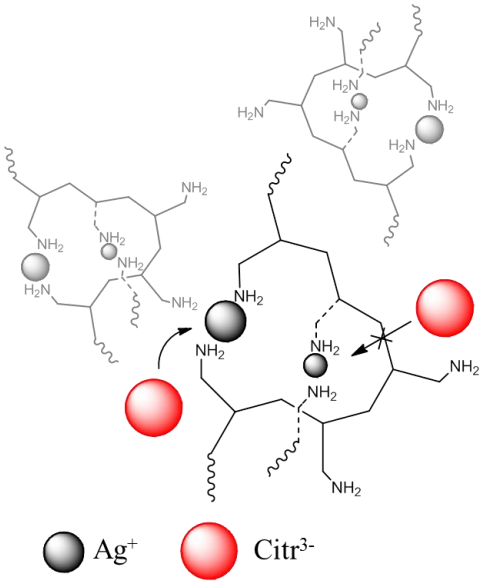

Figure S3. A representative structure showing the molecular structure during the formation of dendritic AgNPs.

Mathematical analysis of dendritic silver particles. Optical images of dendritic silver patterns were analyzed using ImageJ (Fiji version).[2] Fractal box analysis was conducted by converting images to 8 bit and using the "fractal box count" function. The box size was chosen to be 2, 3, 4, 6, 8, 12, 16, 32 and 64. The number of boxes containing a fraction of the image was counted. For fractal structures, such operation should return a linear trend in the box number-log(box size) plot. We noted that all the patterns are perfect dendritic structures, demonstrated by the high R values in linear regression (Table S1). The FD value for various pattern types varied from 1.41 to 1.82 (Table S1). The standard deviation of FD for a specific type of pattern is much

smaller compared with the difference in FD among various pattern types, which makes it possible to readily distinguish pattern types according to FD.

To count the number of branches and junctions in an image, the 8 bit image was first skeletonized and then analyzed using the "analyze skeleton" function. The skeletonization function takes the line between two adjacent junctions (or one junction and one end) as a branch. Here, the junction/end was defined as a voxel that had more than two/only one neighbor(s), respectively. We used the shortest branch method and pruned the ends to eliminate loops and end-points, respectively. To ensure accuracy, at least three images were analyzed for each type of pattern.

Table S1. Fractal dimension of various dendritic Ag patterns

Pattern type	**I**	**II**	**III**	**IV**	**V**
FD	1.716±0.013	1.671±0.017	1.571±0.046	1.41±0.058	1.821±0.015
R^2	0.998	0.999	0.999	0.998	0.999

It is expected that different level of branches will be observed in dendritic patterns, corresponding to the order of silver growth (Figure S4). The smallest n^{th} level branch will be due to Ag nanoparticles that attach to the Ag nanowire network. The number of branches will increase as one progresses to higher levels. It is found that the branch density increased following a near-exponential trend as the FD increased (Figure S5). This is easy to understand as FD is a measurement of surface coverage and follows a scaling rule[3]

$$N = \epsilon^{-FD}$$

where the variable N stands for the number of segments, and ε is the scaling factor (normally smaller than 1). The only deviation was found in type I patterns, which might be due to the fact that some branches were thicker than those in other patterns.

When the N/Ag was changed, the relative reaction rate of step 1 and 2 would alter, leading to variations in branch/junction densities and distinctive branch length distributions (Figure 5a-5e). For type I and type II patterns, the branch length distribution can be fitted by a single Gaussian function with the peak centers located at 1.3 μm and 1.5 μm, respectively. Compared with type I patterns, the branches in the type II pattern had a narrower distribution. An additional Gaussian peak was observed in type III patterns at 4.2 μm and type IV patterns at 5.4 μm, which corresponded to longer branches. This indicated that the growth speed of the Ag crystals exceeded the seeding speed under those conditions. Note the longest branches could only exist as first level branches due to steric effects (Figure S4). As a result, the major portion of branches still featured a shorter length. The average branch length dropped to 0.8 μm for type V pattern. We believe this was due to the insufficiency of free silver ions as most silver ions would be chelated by the amine groups on PAAm, which hindered crystal growth. The average branch length (L) generally reflected the same findings (Figure 5f). To analyze the branching characters in dendritic Ag patterns, we define a parameter w, which is the weighted number of branches at a specific length. By definition, $= N_L \times L$, where N_L is the number of branches with length L. The value of w represents the total length of Ag that grows into a specific type of branch. Each type of dendritic pattern can be distinguished by the distribution of w as a function of

branch length (Figure S6a-S6e). In the *w-L* plot, several linear trends can be observed for each type of dendritic structure. The slope of the linear trends represents N_L and for each linear trend N_L is the same. In addition, the linear trend with lower slope always possesses greater average length. We believe that each linear trend represents one level of branch. The trend with the smallest slope comes from level 1 branching, which is the major branch that first forms in the solution. Similarly, the trend with the second, third, …, m^{th} smallest slope will be level 2, 3, …, m branches. The number of distinguishable linear trends indicates how many times the structure copies itself. For type II, III and IV patterns, four levels of branches are identified, demonstrating a significant complexity. For type I and V, three levels are observed, indicating a lower complexity.

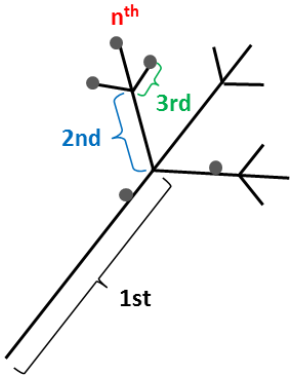

Figure S4. Branch identification in skeleton analysis. Different levels of branch were labelled in the image according to the growth process.

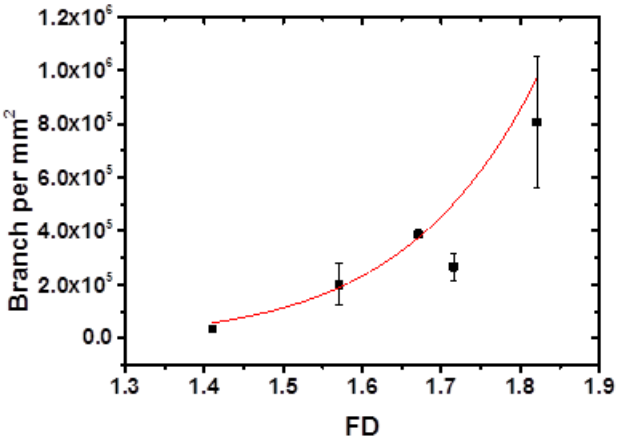

Figure S5. The branch density as a function of FD.

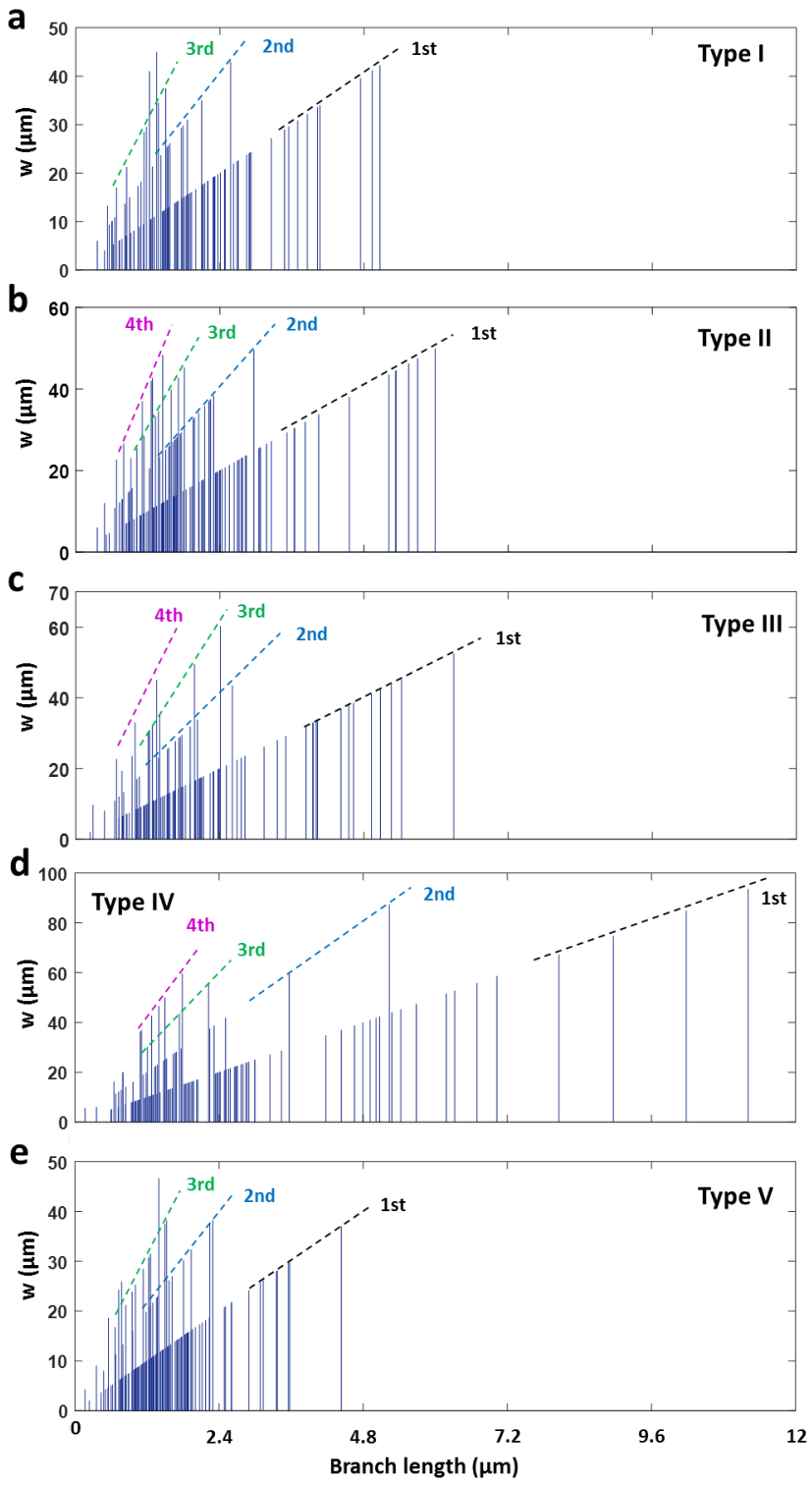

Figure S6. (a)-(e) w-L plot of 5 types of dendritic patterns in Figure 3(b)-(f).

Anti-counterfeiting labelling. A SIFT analysis was performed to extract feature points from the tags and the keys, and to compare them using a program previously developed by us.[1] It was found that all the keys selected from tag I could be readily identified as a good match to tag I. On the other hand, key 5 selected from tag II didn't show any match to tag I, although both tags were generated from the same batch of Ag dendrites. The number of corresponding features found in the identification process was listed in table S2. The identified matching points showed no or very little displacement from the original features in the image.

Table S2. Parameters obtained from the identification process

Event	Matching feature number	Average displacement (pixel)	Identified
Tag I-key 1	69	0.16	Yes
Tag I-key 2	27	0	Yes
Tag I-key 3	150	0	Yes
Tag I-key 4	213	0	Yes
Tag I-key 5	0	N.A.	No

References

1 A. Valehi, A. Razi, B. Cambou, W. Yu, M. Kozicki, in *Computing Conference 2017*, IEEE, **2017**, pp. 863-870.

2 J. Schindelin, I. Arganda-Carreras, E. Frise, V. Kaynig, M. Longair, T. Pietzsch, S. Preibisch, C. Rueden, S. Saalfeld, B. Schmid, J. Y. Tinevez, D. J. White, V. Hartenstein, K. Eliceiri, P. Tomancak, A. Cardona (2012). Fiji: an open-source platform for biological-image analysis. *Nature methods* **2012**, 9, 676.

3 P. M. Iannaccone, M. Khokha, *Fractal geometry in biological systems: an analytical approach*, CRC Press, Boca Raton, USA, **1996**.